Origin of the Neoproterozoic Baijianshan banded iron formation at the southeastern margin of the Tarim Block in NW China: implication for an extremely reducing ocean

Xiao-Shu Hao Chuan-Lin Zhang* Hui-Chao Zhang Teng Ding Xian-Tao Ye

College of Oceanography, Hohai University, Nanjing 210098, P.R. China

Abstract: The Neoproterozoic Banded iron formations (BIFs) were closely associated with the during the breakup of the Rodinia, thus they played an important role in our understanding of the atmospheric and oceanic oxygen levels during this period. In this contribution, the Neoproterozoic (ca. 737 Ma) Baijianshan BIF at Southeast Tarim, northwestern China was identified. Magnetite is the dominated iron-species, which occurs as the lamina interbedded with chert. The BIF contains low concentrations of trace elements, and is depleted in light rare earth elements (LREEs) based on comparison with the Post Archean Australian Shale (PAAS). In addition, the BIF exhibits slightly positive La-Eu anomalies, negligible Ce anomalies, insignificant Y anomalies, chondritic Y/Ho ratios (23-32), and slightly chondritic initial -0.45 to 1.46, averaging 0.37). All these features indicate that the precipitation of Baijianshan BIF was closely related to the submarine low-T hydrothermal fluids with little detrital contribution. Moreover, the Baijianshan BIF is $^{57}Fe_{IRMM-014}$ values ranging revealing the partial oxidation of Fe^{2+} into Fe^{3+} during the precipitation of this BIF. Our data suggest that the formation of Baijianshan BIF was closely associated with a significantly reducing ocean, which most likely was isolated from the oxidized atmosphere by a local ice sheet. This Neoproterozoic Baijianshan ocean has the initial oxygen levels as low as, or even lower than that of Archean and Paleoproterozoic oceans.

Key words: Neoproterozoic, banded iron formations (BIFs), Sr-Nd isotope, Fe isotope, Tarim block

*Corresponding Author: E-Mail: zhangchuanlin@hhu.edu.cn

1 Introduction

Banded iron formations (BIFs), f the most important iron sources in the world, are typical marine sedimentary rocks mainl ted during the Precambrian. BIF was firstly defined as a type of sedimentary rock contai n 15% iron (James, 1954, 1966), which was later revised as thinly layered or lamina chert (or its metamorphic equivalent) alternating with layers that are composed r ls with the iron content ranging from 20% to 35% (James, 1983). The olde .8 Ga (Isua, Greenland), and then a large number of BIFs formed duri oic (3.5-1.8 Ga), with a peak at ca. 2.5 Ga (Klein, 2005 and the refer at ca. 1.8 Ga, and reoccurred in the Neoproterozoic (0.8-0.6 Ga) 05). It is commonly accepted that the precipitations of BIFs ges in atmospheric and/or oceanic oxygen levels (i.e., Great key issues, including the source of the hydrothermal fluids, still under debate (Holland, 2002). In line with tectonic ided into Algoma- and Superior-type (Gross, 1980), the y the volcano craters, in the sequences mainly composed of s (Klein and Beukes, 1992; Li et al., 2014; Sial et al., 2015), med with sedimentary rock in shallow marine environment, and Mcleod, 1980).

ozoic BIFs are even much less than those of Archean and uted worldwide, such as Rapitan BIF in Canada (Halverson et F in Egypt (Basta et al., 2011), Sawawin BIF in Saudi Arabia (Freitas et al., 2011), Holowilena and Oraparinna in South n Peak Formation in California (Lechte et al., 2018) and Wadi (El-Rahman et al., 2020). They were also discovered in the rogenic belts of South China, such as Sanjiang in Guangxi nan Province (Xu et al., 2014), Xinyu in Jiangxi Province (Li et al., 2019), the Shalong in the Central Tianshan (Lei et al., 2016, 2018) and Western Kunlun orogenic belt (Hu et al., 2017, 2020). Several

14801.

fractions and then zircon grains were hand-picked

data are

were carefully selected along the geological location. Whole-rock major compos were analyzed using standard X-ray fluorescence (XRF) on Mineral Resources (China Geological

Fe_2O_3,

HNO_3 in screw top PT

than 200 ppm. The analytical

Institute of Geology and Mineral Rese

for mass-fractionation using $^{86}Sr/^{88}Sr = 0.1194$

values for the NBS SRM 987 standard $^{87}Sr/^{86}Sr$

$^{143}Nd/^{144}Nd = 0.512115$. All the initial $^{143}Nd/^{144}Nd$ value

depositional age (737 Ma) for the Baijianshan BIF.

Iron isotope ratios were measured using MC-ICP-MS at Beijing

$^{57}Fe_{CAGS}$

Accepted Artic

5 Analytical Results

5.1 Zircon U-Pb age

Zircons from the tuff sample 2071 are variable in size with the length varying from 60 μm to 150 μm and the aspect ratios 1-2. In CL images most zircon exhibit oscillatory zoning, sharing the features of the zircons crystallized from silicic magma (Wu and Zheng, 2004). Thirty-two analyses were conducted on 32 zircon grains and the results are presented in supplementary Table 1 and illustrated in Fig. 4. Obviously, some analyses show variable radiogenetic lead lost. However, the results can be broadly divided into two sub-groups. Group 1, which is likely to be xenocrystal and generally have larger size, constructs a good Discordia with upper intercepted age of 1378±44 Ma (MSWD=5.8). Group 2 mostly shows euhedral in form and smaller in size. Twenty-one analyses construct a good Discordia with an intercepted age of 736.2±3.8 Ma (N=21, MSWD=1.08) (insert of Fig. 4). Excluded the significant discordant analyses, the left fifteen analyses of well concordance between $^{206}Pb/^{238}U$ age and $^{207}Pb/^{235}U$ age, yield a mean $^{206}Pb/^{238}U$ age of 737.0±4.0 Ma (N=15, MSWD=0.20). This age is interpreted as the deposition time of the Baijianshan BIF.

5.2 Whole rock Geochemistry

5.2.1 Geochemistry of the basalts

Three basalt samples (2702H1, 270H2 and 2702H3) have low SiO_2 contents (39.93% to 44.55%). The incompatible elements for the rock type classification are used due to the high LOI. Their high Nb/Y ratios (1.05-1.09) define their alkaline signature and in the Nb/Y vs. Zr/TiO_2 diagram, they plot into the alkaline basalt field (Figure not shown). With respect to the trace elements, they have REE ranging from 186 ppm to 195 ppm and show variable LREE enriched Chrondrite-normalized pattern (Fig. 5a) (La_N/Yb_N = 9.8-11.0). In line with their low Cr (214-306 ppm) and Ni contents (162-216.9 ppm), the basalts are evolved magma. However, the primitive mantle-normalized diagram shares most features of the OIB-like basalts with insignificant Nb-Ta trough (Nb/La = 1.0-1.1) (Figure not shown).

5.2.2 Geochemistry of the BIF

As shown in supplementary Table 2, the samples from Baijianshan BIF are rich in $Fe_2O_3^T$ and SiO_2. $Fe_2O_3^T$ concentrations vary between 13.11% and 56.65% (38.44% on average), whereas SiO_2 varies between 26.81% and 55.06% (42.02% on average). They have low contents of Al_2O_3 (1.56%-7.58%, 3.66% on average), TiO_2, MnO, P_2O_5, CaO, Na_2O, K_2O and variable total rare earth elements and other incompatible elements (supplementary Table 2).

Their REE abundances vary from 38.1 ppm to 150.8 ppm. Normalized against Post Archean Average Shale (PAAS; McLennan, 1989), they are characterized by depletion of LREE relative to HREE with the La_N/Yb_N of 0.23-0.69 (Fig. 5b). The REY patterns exhibit no Ce and Pr anomalies (the combination of $Ce/Ce^* \sim 1$ and $Pr/Pr^* \sim 1$; Bau and Dulski, 1996) and insignificant Eu and Y anomaly (Eu/Eu^* = 0.96-1.14; Y/Ho ratios ranging from 23.3 to 31.8 with an averaged value of 26.39, Table 2).

5.2.3 Sr-Nd isotope compositions

Sr-Nd concentrations and isotopic ratios of the Baijianshan BIF and basalts are presented in supplementary Table 3. As for the basalts, the basalts exhibit high initial Sr isotope compositions with $(^{87}Sr/^{86}Sr)_i$ ranging from 0.7061 to 0.7084 due to post-eruption hydrothermal alteration. In addition,

6.9.

Strontium and neodymium concentrations of Baijianshan BIF range from 20.3 ppm to 256 ppm and from 7.06 ppm to 59.8 ppm, respectively. The nine samples have a large range of measured $^{143}Nd/^{144}Nd$ (0.51231-0.51243) and $^{87}Sr/^{86}Sr$ (0.7179- (t = 737Ma) values range from -0.45 to 1.46, with an average of 0.37. However, the BIF samples exhibit a large range of the $(^{87}Sr/^{86}Sr)_i$ values between 0.6412 and 0.7175, possibly due to the post-deposition hydrothermal alteration and the large range of Rb/Sr ratios varying from 0.02 to 3.47.

5.2.4 Fe isotope compositions

The Fe isotope compositions of the Baijianshan BIF samples are presented in supplementary Table 4. The six samples yield $^{56}Fe_{IRMM-014}$ values of 1.24- $^{57}Fe_{IRMM-014}$ values of 1.78- Their enrichment in heavy Fe isotopes shares the signatures of the Neoproterozoic BIFs (Halverson et al., 2011; Yan et al., 2011; Shen et al., 2018).

6 Discussions

6.1 Iron sources for the Baijianshan BIFs

Field and microscopic observations revealed that the Neoproterozoic Baijianshan BIF has not

experienced significant metamorphism (Fig. 3b, c and d), indicating the original geochemical characteristics were well retained and can be used to decipher the iron sources and the oceanic environments when it precipitated.

The Baijianshan BIF shows a modern seawater REE signature with significant LREE depletion relative to the HREE (La_N/Yb_N = 0.41) (Fig. 5b, Zhang and Nozaki, 1996; Alibo and Nozaki, 1999). A range of factors can affect the primary REY composition in terms of BIF depositional processes, including post-depositional metamorphism and/or syn-deposition clastic contamination (Alexander et al., 2008; Hu et al., 2020). Previous studies demonstrated that diagenetic and metamorphic events (such as weathering and/or fluid-rock interactions) have negligible effects on the REY of the chemical sediments (Bolhar et al., 2004). However, Rb is a relatively mobile element compared to highly immobile elements such as Th. In Fig. 6a, the well positive correlation between Rb and Th demonstrates insignificant mobility of the LILEs (Large Ion Lithophile Elements) and the absence of significant diagenetic or metamorphic alteration effects, this conclusion is also consistent with thin section observations (Fig. 3c, d, g, h). With respect to the syn-depositional processes, the contents of Al_2O_3 and TiO_2 are consistently low with averages of 3.66% and 0.41%. In addition, despite the positive correlations between Al_2O_3 and TiO_2 (r = 0.93), K_2O (r = 0.79), Rb (r = 0.78), V (r = 0.45), Sc REE (r = 0.62) (Fig. 6b-i) signify the incorporation of terrigenous contribution in the deposition processes, most correlation coefficients are much lower than those BIFs sourced from recycled crust (Basta et al., 2011; Cox et al., 2013; Hu et al., 2017, 2020). Besides, the Baijianshan BIF shares similar REE patterns with those BIFs from North China Craton but contains slightly higher contents of Al_2O_3 and TiO_2 (Li et al., 2014). Taken together, we suggest a little incorporation of terrigenous component in the Baijianshan BIF.

Positive Eu anomalies are generally interpreted as the precipitation of high-temperature hydrothermal fluids (Danielson et al., 1992; Bau and Dulski, 1999) while low-temperature hydrothermal fluids usually display weak or no Eu anomalies (Michard et al., 1993; Li et al., 2014). Most samples from the Baijianshan BIF show negligible Eu anomalies (Eu/Eu^* = 0.96~1.14, averaging 1.07), which are indicative of low-temperature hydrothermal solutions (Danielson et al., 1992). The (t) value can be used as a tracer to distinguish different sources and crustal contamination. As shown in Fig. 7, the Baijianshan BIF has slightly average (t) value (average of 0.37), much lower than those of Baijianshan basalt, indicating that the deposition of the Baijianshan BIF was controlled by a hydrothermal flux with mantle- (Jacobsen and Pimentel-Klose, 1988). However, the slightly negative correlation between Ma) and Al_2O_3 contents (Fig. 8a) argues for the low proportion of detrital components inputting.

The Y/Ho ratios of BIFs can provide constraints of the material source and precipitation environment of BIFs (Hu et al., 2017). Modern seawaters have a Y/Ho ratio of 44-74 (Bau and Dulski, 1996). The terrestrial material has a Y/Ho ratio of ~26, any little terrestrial contamination could quickly descend seawater-like superchondretic Y/Ho ratios (>44) (Bolhar et al., 2004). The hydrothermal fluids have almost chondritic Y/Ho ratios (26-28, Douville et al., 1999; Bau and Dulski, 1999). The Baijianshan BIF has a range of Y/Ho ratios between 23 and 32, similar to the chondritic values (26-28, Bau and Dulski, 1999), possibly due to the mixture of high and/or low-T hydrothermal fluids (Hu et al., 2020). Y/Ho ratios of the Baijianshan BIF samples might inherit from the low-T hydrothermal fluids, but the influences of terrestrial materials can not be completely excluded. Compared with the BIFs in North China Craton, the Baijianshan BIF displays relatively low positive Eu anomalies, low Y/Ho ratios as well as a slighly depleted Li et al., 2014; Wang et al., 2016), illustrating the input of low-temperature hydrothermal fluids during the deposition of the Baijianshan BIF.

Ce/Ce^*_{PAAS} values with variable Al_2O_3 contents of the Baijianshan BIF indicate that terrigenous detrital materials played little role in the geochemical budget of Ce. In oxidized seawater, Ce(Ⅲ) transforms into Ce(Ⅳ), and then Ce(Ⅳ) is likely to be hydrolyzed and precipitated with Fe-Mn oxyhydroxides, organics and clay which lead to a significant negative Ce anomaly of seawater (Byrne and Sholkovitz, 1996). As shown in the Ce/Ce^* vs. Pr/Pr^* diagram (Fig. 10), all the Baijianshan BIF samples display no Ce anomalies, similar with most Neoproterozoic BIFs, unambiguously arguing for anoxic environment in the ancient ocean. Although the atmospheric and oceanic oxygen levels during the Neoproterozoic are still under debate, numerous studies revealed that Neoproterozoic oceans underwent a stepwise and protracted oxidation. Anoxic ferruginous deep seawater was a typical feature of the late Neoproterozoic, as inferred from geochemical proxies such as iron geochemistry (e.g., Canfield et al., 2008; Sperling et al., 2015), redox-sensitive elements (e.g., Schröder and Grotzinger, 2007; Rajabi et al., 2015), and framboidal pyrite (e.g., Rajabi et al., 2015). Stern et al. (2013) suggested that this scenario might be attributed to the seawater surfaces being covered by ice sheets, blocking the oxygen from atmosphere dissolving into the widespread anoxic ferruginous ocean. Despite no tillite was identified at the Baijianshan BIF, the coeval tillite sequences were documented in the Quruqtagh area (i.e., ca.740 Ma Beiyixi tillite) of NE Tarim (Xu et al., 2009), which argued for the possibility of ice sheets in the Cryogenian Baijianshan ocean.

In a Fe^{2+}-rich marine settings, both abiotic and biotic action were demonstrated as oxidation pathways for the precipitation of iron oxyhydroxides ($Fe(OH)_3$) from dissolved Fe^{2+} (Konhauser et al., 2011). As an element of variable valency, the fractionation of Fe isotope is affected by the oxidation-reduction condition (Bullen et al., 2001; Zhu et al., 2002; Balci et al., 2006). Experimental studies demonstrated that oxidation of Fe^{2+} to Fe^{3+} in solution causes considerable Fe isotope fraction, generating an enrichment of heavy Fe isotopes in Fe^{3+} (Bullen et al., 2001; Johnson et al., 2002; Balci et al., 2006; Hou et al., 2014). On the other hand, the fractionation caused by pyrite with light-Fe isotopes is considered to play a leading role in the enrichment of heavy Fe isotopes in the residual system relative to the original state (Rouxel et al., 2016), since the pyrite is easier to precipitation from plume. Nevertheless, there is no sulfide observed in the Baijianshan BIF, thus the potential influences of sulfides on the enrichment of heavy Fe isotopes can be excluded. Under oxidized environment, the enrichment of heavy Fe isotopes is shown in oxide or hydroxide of iron trivalent (Fe^{3+}_{ppt}) and light Fe isotope is displayed in Ferrous solution (Fe^{2+}_{aq}) (Johnson et al., 2002). The magnitude of Fe isotope fractionation is controlled by the degree of precipitation from Fe^{2+} to Fe^{3+}, which is related to the degree of ocean oxidation (Yan et al, 2010). The Fe in the seawater can be completely precipitated and no fractionation of the Fe isotope occurs when the seawater is completely oxidized, thus the Fe isotope values in iron oxide precipitates (Fe^{3+}) can represent the Fe isotope information of seawater. However, when the seawater is partially oxidized, the Fe in the seawater is partially precipitated and the Fe isotope fractionation will occur in iron oxide precipitates (Fe^{3+}). Therefore, the Fe isotope value can be used as a proxy to decipher the redox state of seawater (Yan et al., 2010). Compared with some BIFs deposited during the Archean-Paleoproterozoic (Dauphas et al., 2004; Rouxel et al., 2005; Li et al., 2012; Johnson et al., 2003; Hou et al., 2014; Li et al., 2014), the Neoproterozoic Baijianshan Sanjiang (Yan et al., 2010) and Xinyu BIFs (Shen et al., 2008) have higher values ^{57}Fe (Fig. 11). Several studies demonstrated that the low ^{57}Fe values of BIFs could be due to the contributions from a continental component and the continental Fe source is best explained by Fe mobilization on the continental margin by microbial dissimilatiry iron reduction (DIR) (Johnson et al., 2008; Li et al., 2015). As for the Fe isotope values of Archean-Paleoproterozoic BIFs we cited, the Fe source of SW Greenland BIF, Anshan-Benxi BIFs, Gongchangling BIFs and Yuanjiacun BIFs are unambiguously demonstrated to be hydrothermal type similar to the scenario of the Baijianshan BIF (Dauphas et al., 2004; Li et al., 2012; Li et al., 2014; Hou et al., 2014), while the Fe of Transvaal, Manjeri, Belingwe Belt and Zimbabwe BIFs are probably from multiple sources (abiologic and biologic processes) (Johnson et al., 2008; Grassineau et al., 2011). The comparison reveals that the environment in which they precipitated was more reduced. Both the iron isotope and elemental geochemistry thus demonstrate that the Neoproterozoic Baijianshan ocean might have the same reduced environment as Archean or Paleoproterozoic, or even more reduced.

6.3 A model of the Baijianshan BIF

During the late Neoproterozoic period (i.e., 750-550 Ma), the Earth experienced long-lived global glaciations, known as the Snowball Earth events (Hoffman et al., 1998). In view of the Neoproterozoic oxygenation event (NOE) at that time, the content of oxygen in atmosphere was much higher than before (Och et al., 2012). Recently, EI-Rahman et al. (2020) argued that some Neoproterozoic BIFs are not glaciogenic due to their significant depleted Nd isotope compositions. Under this scenario, the iron was most likely deriving from hydrothermal alteration of juvenile oceanic crust. The Chondritic-like Nd isotope compositions of the Baijianshan BIF (do not favor this model. Furthermore, the close temporally-spatially related tillite sequences in the Quruqtagh of NE Tarim (Xu et al., 2009), 765 Ma-735 Ma tillites in Namibia, suggested a local glaciation termed as Kaigas

Accepted Article

Cambrian, South China: Petrological, geochronological and stable isotopic constraints. Chemical Geology 258, 168-181.
Cox, G.M., Halverson, G.P., Minarik, W.G., Heron, D.P.L., Macdonald, F.A., Bellefroid, E.J., Strauss, J.V., 2013. Neoproterozoic iron formation: an evaluation of its temporal, environment al and tectonic significance. Chem. Geol. 362, 232-249.
Cox, G.M., Halverson, G.P., Poirier, A., Le Heron, D., Strauss, J.V., Stevenson, R., 2016. A model for Cryogenian iron formation. Earth Planet. Sci. Lett. 433, 280-292.
Danielson, A., Moller, P., Dulski, P., 1992. The europium anomalies in banded iron formations and the thermal history of the oceanic crust. Chem. Geol. 97, 89-100.
Dauphas, N., van Zuilen, M., Wadhwa, M., Davis, A.M., Marty, B., Janney, P.E., 2004. Clues from Fe isotope variations on the origin of early Archean BIFs from Greenland. Science 306, 2077-2080.
EI-Rahman, Y.A., Gutzmer, J., Li, X.H., Seifert, T., Li, C.F., Ling, X.X., Li, J., 2020. Not all Neoproterozoic iron formations are glaciogenic: Sturtian-aged non-Rapitan exhalative iron formations from the Arabian-Nubian Shield. Mineralium Deposita 55, 577-596.
Feng, L.J., Huang, J., Lu, D.B., Zhang, Q.R., 2016. Major and trace element geochemistry of the Neoproterozoic syn-glacial Fulu iron formation, South China. Geological Magazine 154, 1-10.
Freitas, B.T., Warren, L.V., Boggiani, P.C., Almeida, R.P.D., Piacentini, T., 2011. Tectono-sedimentary evolution of the Neoproterozoic BIF-bearing Jacadigo Group, SW-Brazil. Sedimentary Geology 238, 48-70.
Grassineau, N.V., Nisbet, E.G., Bickle, M.J., Fowler, C.M.R., Lowry, D., Mattey, D.P., Abell, P., Martin, A., 2000. Antiquity of the biological sulphur cycle: evidence from sulphur and carbon isotopes in 2700 million-year-old rocks of the Belingwe Belt, Zimbabwe. Proc. R. Soc. Lond. B 268, 113-119.
Gross, G.A., 1980. A classification of iron-formation based on depositional environments. Canadian Mineralogist 18, 215-222.
Gross, G.A., Mcleod, C.R., 1980. A preliminary assessment of the chemical composition of iron formation in Canada. Canadian Mineralogist 18, 223-229.
Halverson, G.P., Poitrasson, F., Hoffman, P.F., Nédélec, A., Montel, J.M., Kirby, J., 2011. Fe isotope and trace element geochemistry of the Neoproterozoic syn-glacial Rapitan iron formation. Earth Planet. Sci. Lett. 309(1), 100-112.
Hoffman, P.F., Kaufman, A.J., Halverson, G.P., Schrag, D.P., 1998. A Neoproterozoic snowball Earth. Science 281, 1342-1346.
Hoffman, P.F., Schrag, D.P., 2002. The snowball earth hypothesis: testing the limits of global change. Terra Nova 14(3), 129-155.
Hoffmann, K.H., Condon, D.J., Bowring, S.A., Prave, A.R., Fallick, A., 2006. Lithostratigraphic, carbon (^{13}C) isotope and U-Pb zircon age constraints on early Neoproterozoic (ca. 755 Ma) glaciation in the Gariep Belt, southern Namibia. Snowball Earth Conference, July 16-21, 2006, Montle Namibia, Ticino, Switzerland, 51.
Holland, H.D., 2002. Volcanic gases, black smokers, and the great oxidation event. Geochimica et Cosmochimica Acta 66(21), 3811-3826.
Hou, K.J., Li, Y.H., Gao, J.F., Liu, F., Qin, Y., 2014. Geochemistry and Si-O-Fe isotope constraint on the origin of banded iron formations of the Yuanjiacun Formation, Lvliang Group, Shanxi, China. Ore Geology Reviews 57, 288-298.
Hu, J., Wang, H., Wang, M., 2017. Geochemistry and origin of the Neoproterozoic Dahongliutan banded iron formation (BIF) in the Western Kunlun orogenic belt, Xinjiang (NW China). Ore Geology Reviews 89, 836-857.
Hu, J., Wang, H., Zhang, L.G., 2020. A rare earth element and Nd isotopic investigation into the provenance and deposition of the Dahongliutan banded iron formation and associated carbonates, NW China: Implications on Neoproterozoic seawater compositions. Precambrian Research 342, 1-29.
Jackson, S.E., Pearson, N.J., Griffin, W.L., Belousova, E.A., 2004. The application of laser ablation-inductively coupled plasma-mass spectrometry to in situ U Pb zircon geochronology. Chemical Geology 211(1-2), 47-69.
Jacobsen, S.B., Pimentel-Klose, M.R., 1988. Nd isotopic variations in Precambrian banded iron formations. Geophys Res Lett 15, 393-396.
James, H.L., 1954. Sedimentary facies of iron-formation. Economic Geology 49(3), 235-293.
James, H.L., 1966. Chemistry of the iron-rich sedimentary rocks. U.S. Geol. Survey Prof, 440-461.
James, H.L., 1983. Distribution of banded iron-formation in space and time. Developments in Precambrian Geology 6, 471-490.
Johnson, C.M., Beard, B.L., Beukes, N.J.,
Earth as inferred from Fe isotope studies of banded iron formations from the Transvaal Craton. Contributions to Mineralogy and Petrology 144(5), 523-547.
Johnson, C.M., Beard, B.L., Klein, C., Beukes, N.J., Roden, E.E., 2008. Iron isotopes constrain biologic and abiologic processes in banded iron formation genesis. Geochimica Et Cosmochimica Acta 72(1), 151-169.
Johnson, C.M., Skulan, J.L., Beard, B.L., Sun, H., Nealson, K.H., Braterman, P.S., 2002. Isotopic fractionation between Fe(Ⅲ) and Fe(Ⅱ) in aqueous solution. Earth Planet Sci Lett 195, 141-153.
Johnston, D.T., Poulton, S.W., Dehler, C., Porter, S., Husson, J., Canfield, D.E., Knoll, A.H., 2010. An emerging picture of Neoproterozoic ocean chemistry: insights from the Chuar Group, Grand Canyon, USA. Earth Planet. Sci. Lett. 290, 64-73.
Kay, R.M., Liyungu, A.K., Njamu, F.M., Somwe, V., Banda, J., Mosley, P.N., Armstrong, R.A., 2001. The western arm of the Lufilian Arc in NW Zambia and its potential for copper mineralization. Journal of African Earth Sciences 33, 503-528.
Klein, C., 2005. Some Precambrian banded iron-formations (BIFs) from around the world: Their age, geologic setting, mineralogy, metamorphism, geochemistry, and origins. American Mineralogist 90(10), 1473-1499.
Klein, C., Beukes, N.J., 1992. Time distribution, stratigraphy, sedimentologic setting, and geochemistry of Precambrian iron-formations. In: Schopf, J.W., Klein, C. (Eds.), The Proterozoic Biosphere. Cambridge University Press, Cambridge, 139-146.
Klein, C., Ladeira, E.A., 2004. Geochemistry and mineralogy of Neoproterozoic banded iron-formations and some selected, siliceous manganese formations from the Urucum district, Mato Grosso do Sul, Brazil. Econ. Geol. 99, 1233-1244.
Konhauser, K.O., Kappler, A.K., Roden, E.E., 2011. The microbial role in iron redox and biomineralization reactions. Elements 7, 89-93.

change. Precambr. Res. 239, 79-94.
Sun, S.S., McDonough, W.F., 1989. Chemical and isotopic systematics of oceanic basalts: Implications for mantle composition and processes. Geological Society London Special Publications 42(1), 313-345.
Tang, S.H., Zhu, X.K., Li, J., Yan, B., Li, S.Z., Li, Z.H., Wang, Y., Sun, J., 2016. New Standard Solutions for Measurement of Iron, Copper and Zine Isotope Compositions by Multi-collector Inductively Coupled Plasma-Mass Spectrometry. ROCK AND MINERAL ANALYSIS 35(2), 127-133 (in Chinese with English abstract).
Wu, Y.B., Zheng, Y.F., 2004. A study on the genetic mineralogy of zircon and its restriction on the interpretation of U-Pb age. CHINESE SCIENCE BULLETIN 49(16), 1589 (in Chinese).
Xinjiang Bureau of Geology and Mineral Resources (BGMR), 1993. Regional Geology of Xinjiang Uygur Autonomous Region. Geological Publishing House, Beijing, 8-33 (in Chinese).
Xu, B., Xiao, S.H., Zou, H.B., Chen, Y., Li, Z.X., Song, B., Liu, D.Y., Zhou, C.M., Yuan, X.L., 2009. SHRIMP zircon U-Pb age constraints on Neoproterozoic Quruqtagh diamictites in NW China. Precambrian Research 168, 247-258.
Xu, B., Zou, H.B., Chen, Y., He, J.Y., Wang, Y., 2013. The Sugetbrak basalts from northwestern Tarim Block of northwest China: Geochronology, geochemistry and implications for Rodinia breakup and ice age in the Late Neoproterozoic. Precambrian Research 236, 214-226.
Xu, D.R., Wang, Z.L., Chen, H.Y., Hollings, Pete, Jansen, Nicholas, H., Zhang, Z.C., Wu, C.J., 2014. Petrography and geochemistry of the Shilu Fe Co Cu ore district, South China: Implications for the origin of a Neoproterozoic BIF system. Ore Geology Reviews 57, 322-350.
Xu, Z.Q., He, B.Z., Zhang, C.L., Zhang, J.X., 2013. Tectonic framework and crustal evolution of the Precambrian basement of the Tarim Block in NW China: New geochronological evidence from deep drilling samples. Precambrian Research 235, 150-162.
Yan, B., Zhu, X.K., Tang, S.H., Zhu, M.Y., 2010. Fe isotopic characteristics of the Neoproterozoic BIF in Guangxi Province and its Implications

Accepted Article

Figure captions

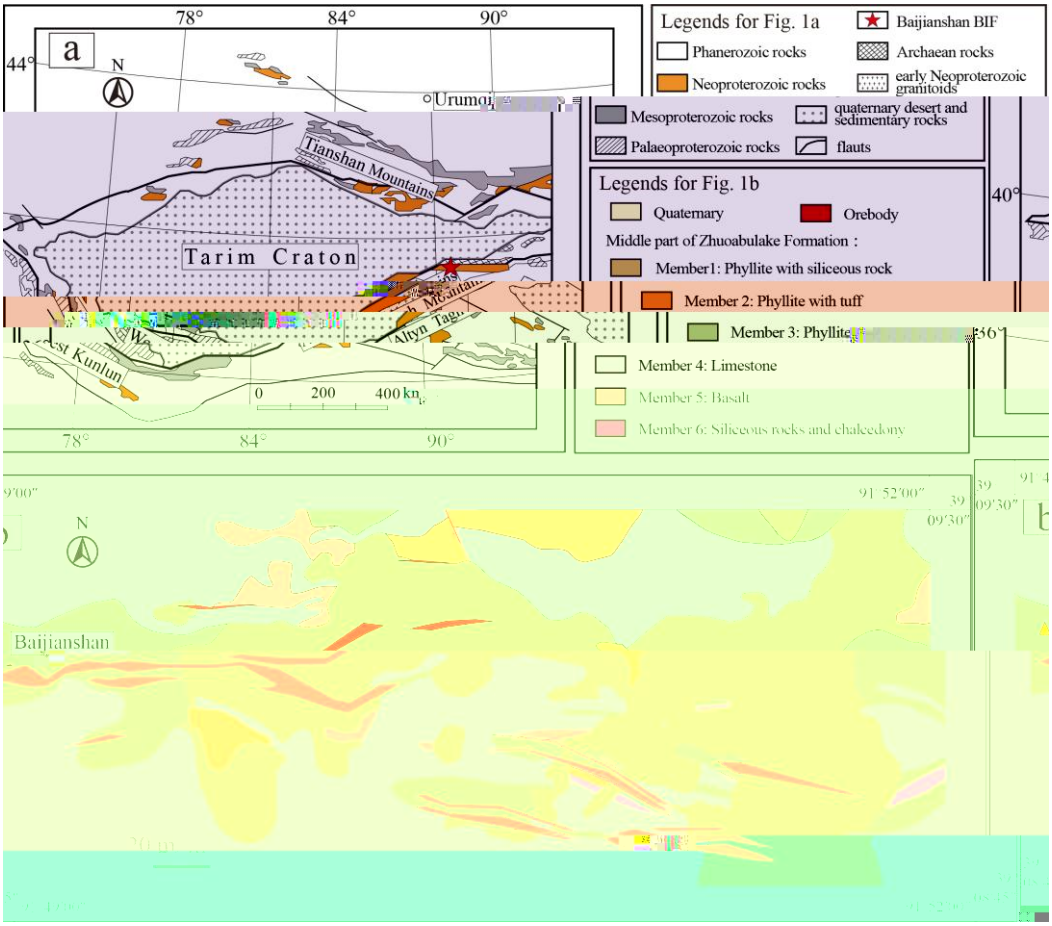

Fig. 1 (a) Sketch Precambrian geological map of Tarim Craton, showing the location of the Baijianshan BIF (modified after Lu et al., 2008). (b) Geological map of the Baijianshan Banded Iron Formation (Baijianshan BIF).

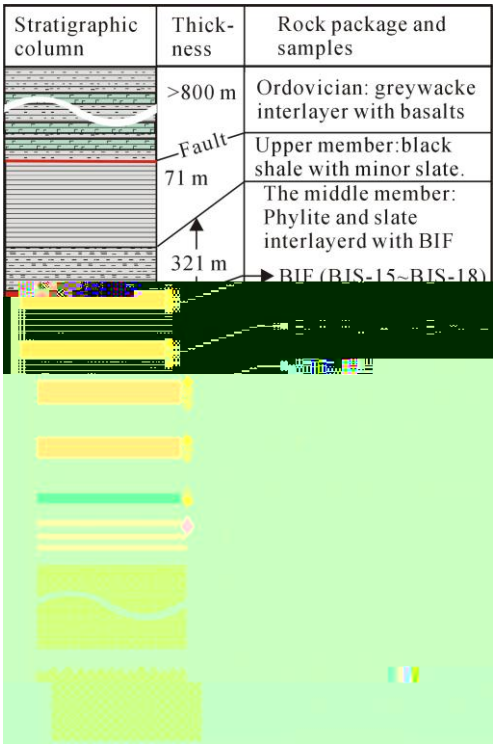

Fig. 2 Stratigraphical column of the Baijianshan BIF.

Accepted Article

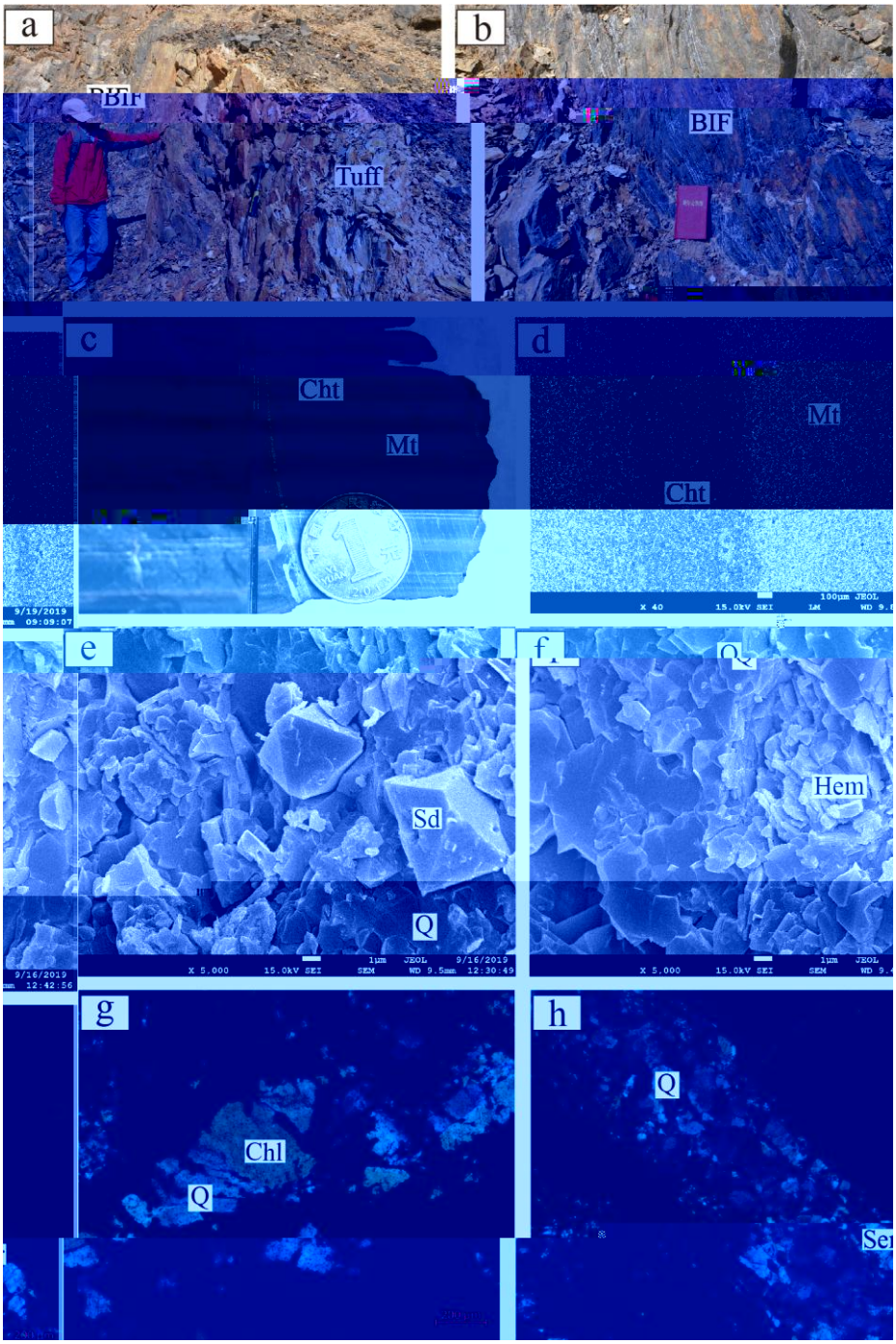

Fig. 3 Field photographs, hand specimen and mineral features of the Baijianshan BIF. (a) The tuff layers in the Baijianshan BIF. (b) Laminated Fe orebodies with local bend. (c) hand specimen. (d) Scanning electron microscopy (SEM) images. Detailed petrographic examination by SEM and transmitted light showing mineral assemblage: (e) Siderite. (f) Hematite. (g) Chlorite. (h) Sericite. Cht = Chert, Mt = Magnetite, Sd = Siderite, Q = Quartz, Hem = Hematite, Chl = Chlorite, Ser = Sericite.

Accepted Artic

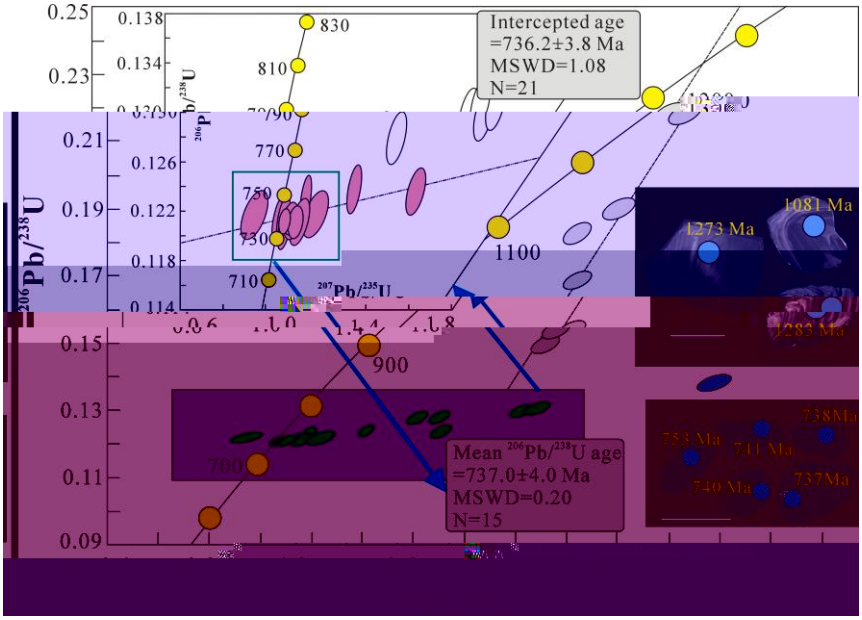

Fig. 4 Concordia diagram of the zircon U-Pb ages of the tuff at the Baijianshan BIF.

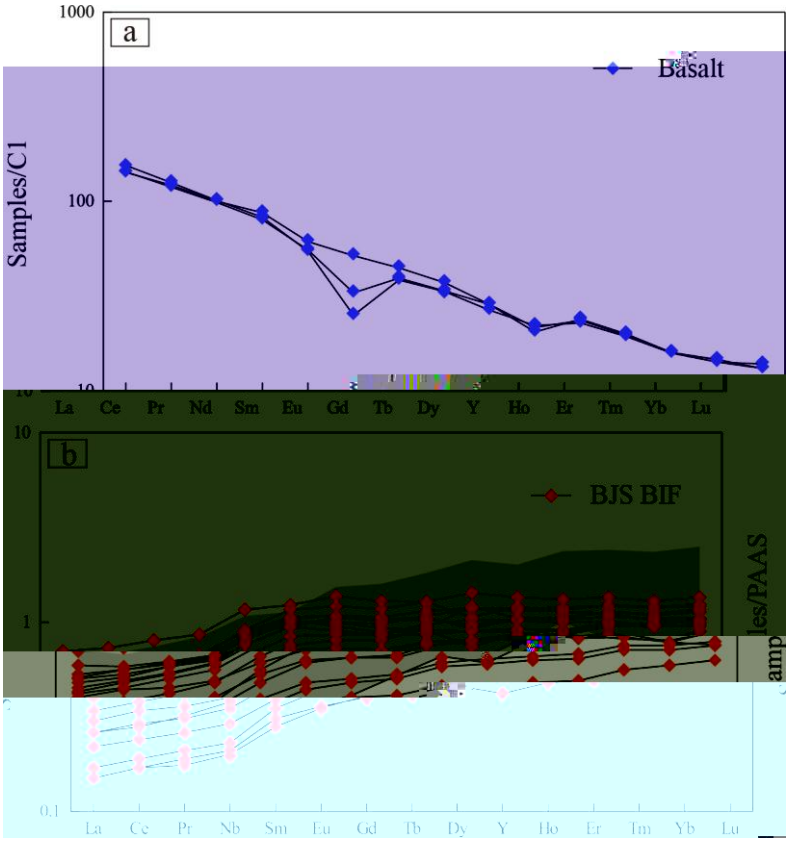

Fig. 5 (a) Chondrite-normalized REE parttern of the basalts. Chondrite-normalized values after Sun and McDonough (1989). (b) PAAS-normalized REE+Y diagrams of BIFs from the Baijianshan BIF. The grayish zone represents the REY data from the Xinyu BIF (Li et al., 2014). PAAS-normalized values after McLennan (1989).

Accepted Article

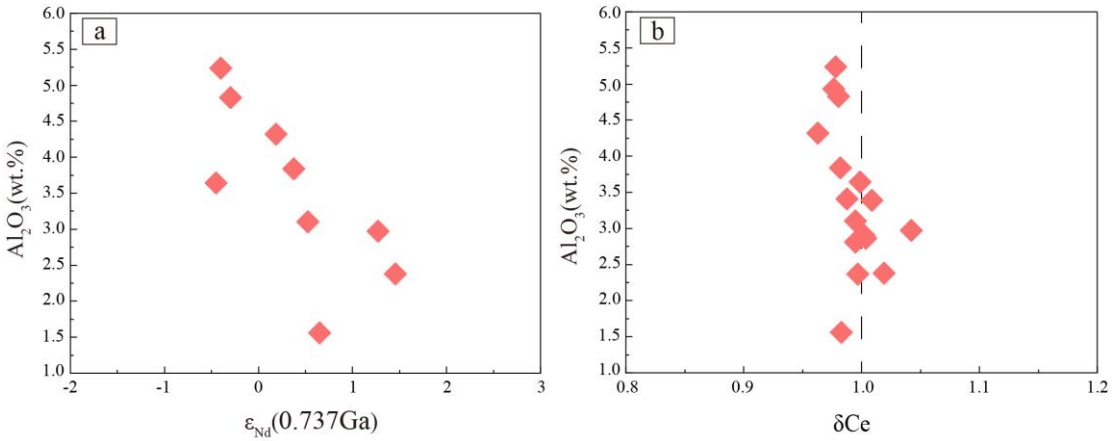

Fig. 8 (t = 0.737Ga) vs. Al_2O_3 diagram of the Baijianshan BIF; (b) Ce/Ce^*_{PAAS} vs. Al_2O_3 diagram of the Baijianshan BIF.

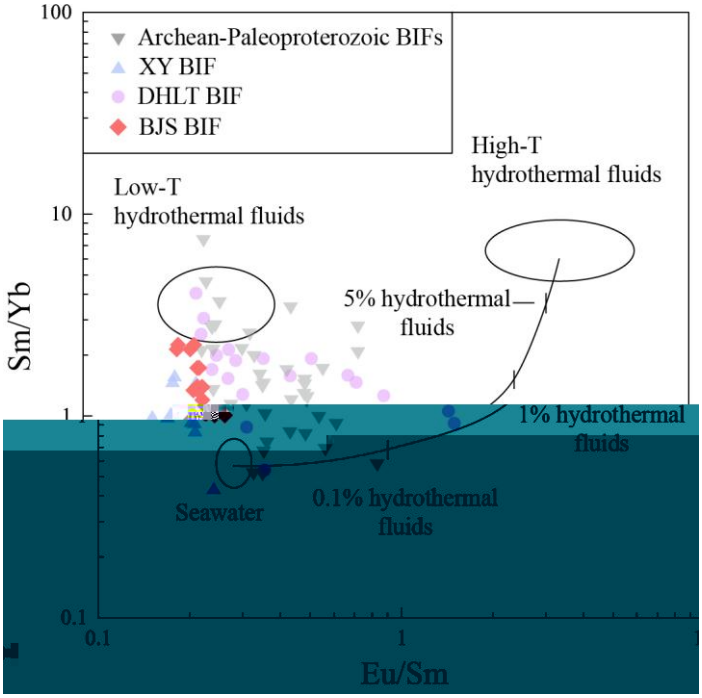

Fig. 9 Sm/Yb vs. Eu/Sm ratios illustrating two component mixing model of the hydrothermal fluid of the Baijianshan BIF (after Alexander et al., 2008). BJS-Baijianshan BIF; XY-Xinyu BIF (Li et al., 2014); DHLT-Dahongliutan BIF (Hu et al., 2017). Data sets of Archean-Paleoproterozoic BIFs are from Planavsky et al. (2010). Average compositions of high-T (> 300 °C) hydrothermal fluids, low-T (< 200 °C) hydrothermal solutions and Pacific seawaters were after Bau and Dulski (1999), Michard et al. (1983) and Alibo and Nozaki (1999), respectively.

Accepted Article

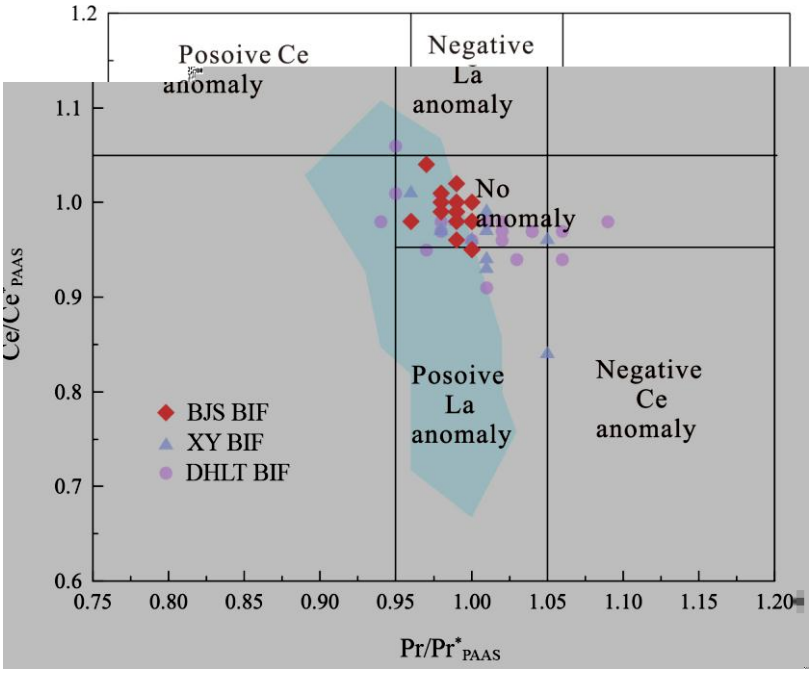

Fig. 10 Pr/Pr^*_{PAAS} vs. Ce/Ce^*_{PAAS} diagram for the BIF at Baijianshan (after Bau and Dulski, 1996). The light blue area represents the data of Archean-Paleoproterozoic BIFs. Data sets of other BIFs are same as those of Fig. 9.

Fig. 11 $^{57}Fe_{IRMM-014}$ of various ages BIFs in the world (Data of SW Greenland BIFs are from Dauphas et al.(2004); Manjeri Formation, Belingwe Belt, Zimbabwe BIFs are from Rouxel et al. (2005); Anshan-Benxi BIFs are from Li et al. (2012); Transvaal BIFs are from Johnson et al. (2003); Yuanjiacun BIFs are from Hou et al. (2014); Gongchangling BIFs from Li et al. (2014); Sanjiang BIF are from Yan et al. (2010) and Xinyu BIF are from Shen et al. (2008)).

Supplementary Table 2 Geochemical compositions of Baijianshan BIF

Sample	BJS-1	BJS-2	BJS-3	BJS-4	BJS-5	BJS-6	BJS-7	BJS-8	BJS-9	BJS-10
Major elements (%)										
Fe_2O_3	53.60	41.52	56.64	52.26	30.01	36.85	41.01	45.22	39.78	48.55
SiO_2	29.91	38.96	26.81	31.20	40.92	40.79	36.97	41.77	43.66	37.59
Al_2O_3	1.56									

Accepted Article

TFe_2O_3	21.79	28.86	44.82	42.63	26.98	13.11	40.45	11.61	11.70	11.98
SiO_2	55.06	49.87	41.24	43.65	53.64	59.90	42.80	39.94	40.91	44.55
Al_2O_3	5.24	4.93	2.81	2.86	4.83	7.58	3.84	11.36	11.45	10.76
CaO	0.81	1.02	0.75	0.75	0.76	0.84	0.65	9.77	9.31	7.45
MgO	1.57	1.51	0.74	0.86	1.36	2.32	1.31	8.40	8.54	10.38
TiO_2	0.60	0.53	0.35	0.25	0.59	0.86	0.41	3.66	3.80	3.60
MnO	0.03	0.04	0.05	0.03	0.03	0.02	0.03	0.24	0.25	0.23
P_2O_5	0.20	0.35	0.49	0.40	0.23	0.19	0.54	0.46	0.43	0.38
K_2O	3.11	2.32	0.26	0.17	1.86	3.78	1.98	1.35	1.27	0.36
Na_2O	0.94	1.25	0.14	0.19	0.63	0.77	0.88	0.94	0.98	0.59
LOI	2.06	1.97	4.57	2.89	2.9	3.19	1.92	12.02	11.39	9.60
FeO	7.97	7.26	3.89	5.29	6.06	6.57	5.31	-	-	-
Total	99.38	99.91	100.11	99.97	99.87	99.13	100.12	99.75	100.03	99.88
Trace elements (ppm)										
Cr	118	81.0	59.7	10.5	86.2	112	50.9	214	214	306
Ni	15.6	14.5	12.1	11.0	15.6	12.3	12.6	162	166	217
Co	76.1	70.2	33.7	34.7	54.0	27.1	45.3	48.0	62.9	50.7
Sc	12.2	14.4	7.97	8.11	11.7	15.1	8.11	26.4	26.1	25.7
Ba	662	562	111	19.2	359	1219	385	877	864	296
Sr	45.0	53.3	45.8	26.1	32.6	37.0	48.9	205	209	150
Rb	111	95.6	7.36	6.13	113	184	85.6	34.4	32.2	12.3
Zr	101	93.4	60.0	87.9	79.9	116	79.7	259	251	228
Hf	2.63	2.37	1.23	1.50	2.11	2.99	1.92	5.35	5.74	6.00
Ta	0.88	0.75	0.37	0.36	0.64	0.84	0.53	2.24	2.33	2.14
Ga	7.95	7.63	4.39	4.63	7.12	10.3	5.97	18.3	17.2	18.8
Cu	27.6	21.6	8.12	3.56	21.4	36.0	12.4	-	-	-
Zn	62.1	40.0	26.0	23.8	35.3	37.0	29.6	-	-	-
Pb	7.80	8.24	3.54	5.32	7.64	15.4	5.75	-	-	-
U	0.47	0.69	0.39	0.40	0.72	0.82	0.37	1.45	1.09	0.92
Th	7.26	5.14	2.81	2.97	5.52	7.11	4.11	3.32	3.37	3.18
Nb	8.35	8.21	4.19	4.86	6.80	9.50	6.11	38.0	36.5	33.6
La	26.8	20.3	13.0	9.82	19.1	22.5	17.3	36.9	34.1	33.7
Ce	58.3	44.2	30.2	22.8	42.0	46.1	39.0	77.2	72.9	74.9
Pr	7.03	5.35	3.73	2.77	5.09	5.51	4.81	9.37	9.15	9.28
Nd	29.3	22.4	16.2	11.7	21.3	22.6	20.7	37.9	36.6	40.0
Sm	6.46	4.95	3.67	2.65	4.70	4.96	4.70	8.06	8.20	9.11
Eu	1.33	1.15	0.91	0.66	1.06	1.01	1.12	1.41	1.85	2.91
Gd	6.39	5.03	4.02	3.03	4.64	4.93	5.01	7.69	7.82	8.87
Tb	1.00	0.80	0.67	0.52	0.72	0.79	0.82	1.21	1.22	1.35
Dy	5.98	4.98	4.53	3.71	4.26	4.84	5.36	6.57	7.04	7.04
Y	28.5	24.9	27.9	22.0	20.1	26.1	31.9	34.8	34.0	32.1
Ho	1.20	1.04	1.02	0.85	0.86	1.01	1.17	1.25	1.29	1.31
Er	3.23	2.94	3.00	2.59	2.33	2.82	3.38	3.11	3.15	3.20
Tm	0.45	0.43	0.46	0.40	0.34	0.41	0.50	0.39	0.40	0.39
Yb	2.87	2.93	3.06	2.76	2.20	2.69	3.36	2.28	2.36	2.28
Lu	0.43	0.45	0.49	0.45	0.33	0.41	0.53	0.34	0.32	0.32
	150.77	116.95	84.95	64.71	108.93	120.58	107.75	193.68	186.4	194.67
Y/Ho	23.75	23.94	27.35	25.76	23.29	25.84	27.26	27.84	26.36	24.50
La/La*	1.06	1.07	1.09	1.02	1.06	1.09	1.10	1.14	1.06	1.14
Ce/Ce*	0.98	0.98	0.99	1.00	0.98	0.95	0.98	0.98	0.98	1.01
Y/Y*	0.85	0.88	1.04	0.99	0.84	0.95	1.02	0.89	0.83	0.78
Pr/Pr*	1.00	1.00	0.99	0.99	1.00	1.00	0.99	0.97	0.99	0.95
Eu/Eu*	0.97	1.08	1.10	1.08	1.07	0.96	1.08	0.54	0.69	0.97
La_N/Yb_N	0.69	0.51	0.31	0.26	0.64	0.62	0.38	10.99	9.82	10.04

Supplementary Table 3 Sr-Nd isotopic data of the Baijianshan BIF

Sample	$^{87}Rb/^{86}Sr$	$^{87}Sr/^{86}Sr$		$(^{87}Sr/^{86}Sr)_i$	$^{147}Sm/^{144}Nd$	$^{143}Nd/^{144}Nd$		T_{DM}(Ga)	
BJS-1	0.0433	0.717927	0.000004	0.7175	0.1457	0.512425	0.000006	1.63	0.65
BJS-4	4.2608	0.727751	0.000009	0.6829	0.1308	0.512394	0.000003	1.39	1.46
BJS-5	1.4305	0.728893	0.000008	0.7138	0.1378	0.512363	0.000003	1.58	0.19
BJS-7	2.4192	0.729423	0.000009	0.7040	0.1473	0.512376	0.000002	1.78	-0.45
BJS-8	2.8555	0.718681	0.000003	0.6886	0.1238	0.512351	0.000004	1.36	1.27
BJS-10	2.6390	0.723954	0.000005	0.6962	0.1344	0.512364	0.000002	1.51	0.53
BJS-12	7.0891	0.740795	0.000007	0.6662	0.1333	0.512311	0.000003	1.59	-0.40
BJS-16	9.9936	0.746329	0.000008	0.6412	0.1334	0.512317	0.000003	1.58	-0.30
BJS-18	5.0054	0.731954	0.000008	0.6793	0.1373	0.51237	0.000004	1.56	0.38
2702H1	0.4737	0.711034	0.000009	0.7061	0.1286	0.512662	0.000003	0.88	6.90
2702H2	0.4355	0.711156	0.000009	0.7066	0.1354	0.512694	0.000006	0.89	6.88
2702H3	0.2322	0.710822	0.000012	0.7084	0.1377	0.512644	0.000005	1.02	5.69

Supplementary Table 4 Fe isotopic data of the Baijianshan BIF

Sample	$^{57}Fe_{IRMM-014}$	$^{56}Fe_{IRMM-014}$